Phase diagram of the chiral magnet Cr1/3NbS2 in a magnetic field

doi: https://doi.org/10.1103/PhysRevB.93.104402

Phase diagram of the chiral magnet $Cr_{1/3}NbS_2$ in a magnetic field

K. Tsuruta,[1,*] M. Mito,[1,†] H. Deguchi,[1] J. Kishine,[2] Y. Kousaka,[3,4] J. Akimitsu,[3,4,5] and K. Inoue[3,4,6]

[1]*Graduate School of Engineering, Kyushu Institute of Technology, Kitakyushu 804-8550, Japan*

[2]*Graduate School of Arts and Sciences, The Open University of Japan, Chiba 261-8586, Japan*

[3]*Graduate School of Science, Hiroshima University, Higashihiroshima 739-8526, Japan*

[4]*Center for Chiral Science, Hiroshima University, Higashihiroshima 739-8526, Japan*

[5]*Department of Physics and Mathematics, Aoyama Gakuin University, Sagamihara 229-8558, Japan*

[6]*Institute for Advanced Materials Research, Hiroshima University, Higashihiroshima 739-8526, Japan*

(Received 26 November 2015; revised manuscript received 2 February 2016; published 1 March 2016)

We construct the phase diagram of the chiral magnet $Cr_{1/3}NbS_2$ in a dc magnetic field (H_{dc}) using ac magnetic susceptibility measurements. At $H_{dc} = 0$, the ac response at the transition from the helical magnetic (HM) state to the paramagnetic (PM) state consists of a giant third-order harmonic component ($M_{3\omega}$) and a first-order harmonic component ($M_{1\omega}$). By applying H_{dc} perpendicular to the c axis, the HM state is transformed to the chiral soliton lattice (CSL) state, which is a superlattice tuned by H_{dc}. The above giant $M_{3\omega}$ is markedly suppressed at small H_{dc}. The CSL state is found to consist of CSL-1, with dominant helical texture and a poor ferromagnetic array, and CSL-2, with a large ferromagnetic array. The transition between CSL-1 and the PM state causes a linear magnetic response, the dominant component of which is the in-phase $M_{1\omega}$. With increasing temperature, CSL-2 is transformed into the forced ferromagnetic (FFM) state, and ultimately the PM state is reached. The transition between CSL-2 and the FFM state consists of a large $M_{3\omega}$ and large out-of-phase $M_{1\omega}$ as well as in-phase $M_{1\omega}$. The transition between the FMM and PM states also yields a linear magnetic response, like the CSL-1–PM-state transition. Five typical magnetic dynamics in the transitions among the HM state, CSL-1, CSL-2, FFM state, and PM state were identified according to the equivalent dynamical motion equation of a nonlinear spring model.

DOI: 10.1103/PhysRevB.93.104402

I. INTRODUCTION

A magnet with crystallographic chirality (a chiral magnet) allows the asymmetric Dzyaloshinskii-Moriya (D-M) interaction, which stabilizes either left-handed or right-handed helical magnetic (HM) structures owing to competition with the exchange interaction [1,2]. In an HM structure with uniform helicity, spin modulation propagates along the chiral axis, so the phase is coherent over a long range. In these chiral magnets, the magnetic state can be manipulated by applying a dc magnetic field (H_{dc}) perpendicular to the chiral axis. With increasing H_{dc}, a periodic array of domain walls (DWs), called the chiral soliton lattice (CSL), is stabilized [3,4]. The CLS was first proposed by Dzyaloshinskii [3]. This coherent state at finite H_{dc} is a type of superlattice structure, the length of which can be tuned by varying the magnitude of H_{dc} [5,6]. Initially, it was theoretically proposed that the transition between the CSL state and the paramagnetic (PM) state exhibits a characteristic cusp in the magnetization (M) measured as a function of temperature (T) [4], and below the magnetic ordering temperature T_c, the characteristic rapid growth of M with increasing H_{dc} suggests a remarkable increase in one unit length of the superlattice [4]. In 1983, indeed, the latter feature had already been observed in a typical chiral magnet, $Cr_{1/3}NbS_2$, with a helicity length at $H_{dc} = 0$ of 48 nm [7]. In 2012, there was an impressive experiment in which an actual image of the CSL state was observed using Lorenz microscopy, and the diffraction image obtained by small-angle electron diffraction also supported the existence of the CSL state [8]. Much progress has been made recently in understanding the CSL.

In terms of crystallography, in $Cr_{1/3}NbS_2$, Cr^{3+} ions are inserted between hexagonal NbS_2 layers. Insertion of Cr^{3+} does not allow inversion symmetry, so the compound crystallizes as the noncentrosymmetric hexagonal space group $P6_322$ [7,9–12]. The electronic transport and magnetic properties depend on how Cr^{3+} is inserted between the NbS_2 layers [12–14]. The magnetism originates mainly from Cr^{3+} inserted into octahedral holes, and electronic transport mainly arises from Nb occupying two inequivalent sites. The magnetism originating in Cr is structurally correlated with the metallic properties originating in Nb via distortion of the CrS_6 octahedron. The ab plane forms the magnetically easy plane. Various exchange interaction paths along both the intraplane and interplane directions have been suggested theoretically [11]. Furthermore, according to the Lorenz microscopy experiment, a ferromagnetic network develops on the ab plane [8]. A decrease in the magnetic ordering temperature T_c under hydrostatic pressure was observed via an ac magnetic susceptibility measurement [12,15], and this behavior is related to the decrease in the distortion of the CrS_6 octahedron [12]. In single crystals, enhancement of the muon spin precession frequency is observed below approximately 50 K, suggesting a low-temperature change in the magnetic structure [16]. Furthermore, the magnetotransport is known to depend on spin orientation below approximately 50 K [17].

Let us review the CSL state in $Cr_{1/3}NbS_2$. At a finite H_{dc} below a critical field H_c for the forced ferromagnetic (FFM) state at $T = 0$ K, the CSL state is transformed to the FFM state with increasing T, and ultimately the PM state is

*n590901k@mail.kyutech.jp

†mitoh@mns.kyutech.ac.jp

reached. A phase diagram based on these phase transitions has been constructed from both an M-H_{dc} measurement [14] and a magnetoresistance (R) measurement [18]. The M-H_{dc} measurement reveals the boundary between the CSL and the FFM and suggests that the CSL consists of two regions depending on whether dM/dH_{dc} is nearly a constant [14]. On the other hand, the kink or peak in R indicates the CSL-FFM transition, and anomalies in dR/dT indicate the FFM-PM transition [18]. These phase (region) diagrams are not perfectly consistent with each other. Herein, when we consider the spatial uniformity of the spin phase, both the HM and FFM states have a coherent spin phase over infinite spatial scale. In the CSL state, however, the spatial scale between DWs changes as a function of H_{dc}, so the scale of the ferromagnetic spin alignment between DWs changes. Thus, the spatial uniformity of the spin phase decreases dramatically at around zero field, and then it systematically approaches infinity with increasing H_{dc}. The above change in the spin phase uniformity should be responsible for any effect on the sensitivity against an ac magnetic field H_{ac}, and in particular it would be detected in the ac magnetic response of the magnetic domains. In this paper, a series of precise phase boundaries is investigated using ac magnetic susceptibility measurements, and the magnetic dynamics on the boundaries is analyzed according to a method of magnetic diagnostics developed by studying the helical magnet MnP [19]. The physical knowledge obtained there would be helpful for understanding the physical properties of the CSL in more detail.

II. EXPERIMENTAL PROCEDURES

A single crystal of $Cr_{1/3}NbS_2$ was synthesized by a procedure described elsewhere [8]. The ac magnetic response ($M_{n\omega}$) was observed using a superconducting quantum interference device (SQUID) magnetometer (Quantum Design) equipped with an ac measurement option. The frequency f of H_{ac} was 0.1–500 Hz, and the amplitude h was 2.0 or 3.9 Oe. H_{ac} was applied parallel to the easy plane (ab plane, i.e., $H_{ac} \perp c$), and its direction was parallel to the direction of H_{dc}. Thus, H_{ac} modifies the helical structure and the CSL state along the direction perpendicular to the chiral axis. In the measurement at zero H_{dc}, the residual H_{dc} was reduced to a level sufficiently below Earth's field.

Herein, we briefly review the harmonic magnetic responses under $H_{ac} = h \sin \omega t$. M as a function of time (t), $M(t)$, is expanded as follows:

$$M(t) = M_{1\omega} \sin(\omega t + \theta_{1\omega}) + M_{2\omega} \sin(2\omega t + \theta_{2\omega}) + M_{3\omega} \sin(3\omega t + \theta_{3\omega}) + \cdots, \quad (1)$$

where $\omega = 2\pi f$ is the angular frequency, $M_{n\omega}$ (where n is an integer) represents the nth-harmonic component, and $\theta_{n\omega}$ (< 0) is the phase delay of each $M_{n\omega}$ against H_{ac}. For instance, $M'_{1\omega} = M_{1\omega} \cos\theta_{1\omega}$, $M''_{1\omega} = -M_{1\omega} \sin\theta_{1\omega}$, $M'_{2\omega} = M_{2\omega} \cos\theta_{2\omega}$, and $M'_{3\omega} = M_{3\omega} \cos\theta_{3\omega}$. The large $M_{2\omega}$ signal reflects the existence of spontaneous magnetization. The anomaly in $M_{3\omega}$ reflects the formation of magnetic domains; the long-range magnetic order is accompanied by a large phase change, and the glassy state due to frustration between the magnetic moments of the magnetic domains does not have a large phase change [20–25]. Thus, magnetic diagnostics using mainly $M_{3\omega}$ can be valid for the study of the complex magnetic properties [19,26–31]. The quantity $M_{3\omega}/M_{1\omega}$ is called the Klirr factor, and it represents the ratio of the strain in the periodic curve of $M(t)$ [19,32]. The harmonic magnetic response, $M_{n\omega}$, was evaluated via the spectral analysis of the time-dependent SQUID voltage, which is proportional to the magnetic flux detected by the detection coil. The obtained $M(t)$ data can also be analyzed via the ac hysteresis curve $M(H_{ac})$ [19]. For reference, $M''_{1\omega}$ is proportional to the area of the $M(H_{ac})$ hysteresis [19].

III. EXPERIMENTAL RESULTS

A. At zero dc field

Figure 1 shows the temperature dependence of the in-phase $M'_{1\omega}$ (a), out-of-phase $M''_{1\omega}$ (b), and amplitude $M_{3\omega}$ (c) for $Cr_{1/3}NbS_2$ at zero H_{dc} under an ac field with $h = 2.0$ Oe and $f = 0.1$–500 Hz. First, $M'_{1\omega}$ has an anomaly at $T_c = 128$ K. At around $T = 126$–127 K, $M''_{1\omega}$ exhibits a sharp anomaly, where $M''_{1\omega}/M'_{1\omega} \sim 10\%$. For reference, $M_{2\omega}$ shows just a small anomaly of $M_{2\omega}/M_{1\omega} = 0.2\%$, whereas the anomaly in

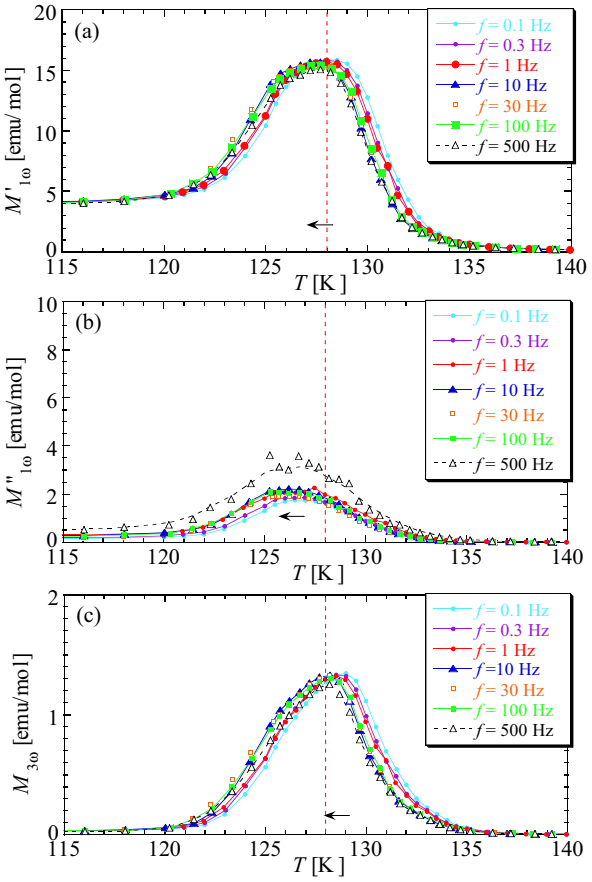

FIG. 1. Temperature dependence of ac magnetic responses (a) $M'_{1\omega}$, (b) $M''_{1\omega}$, and (c) $M_{3\omega}$ for $Cr_{1/3}NbS_2$ at $H_{dc} = 0$ under an ac field with $h = 2.0$ Oe and $f = 0.1$–500 Hz. Both H_{dc} and H_{ac} are applied perpendicular to the c axis. A series of ac responses corresponds to the magnetic response [A] in Fig. 8. Red dotted lines, which represent the temperature with the maximum $M'_{1\omega}$ in the low-frequency limit, are guides for the eyes. Arrows in (a), (b), and (c) indicate the direction of the shift for $M'_{1\omega}$, $M''_{1\omega}$, and $M_{3\omega}$, respectively.

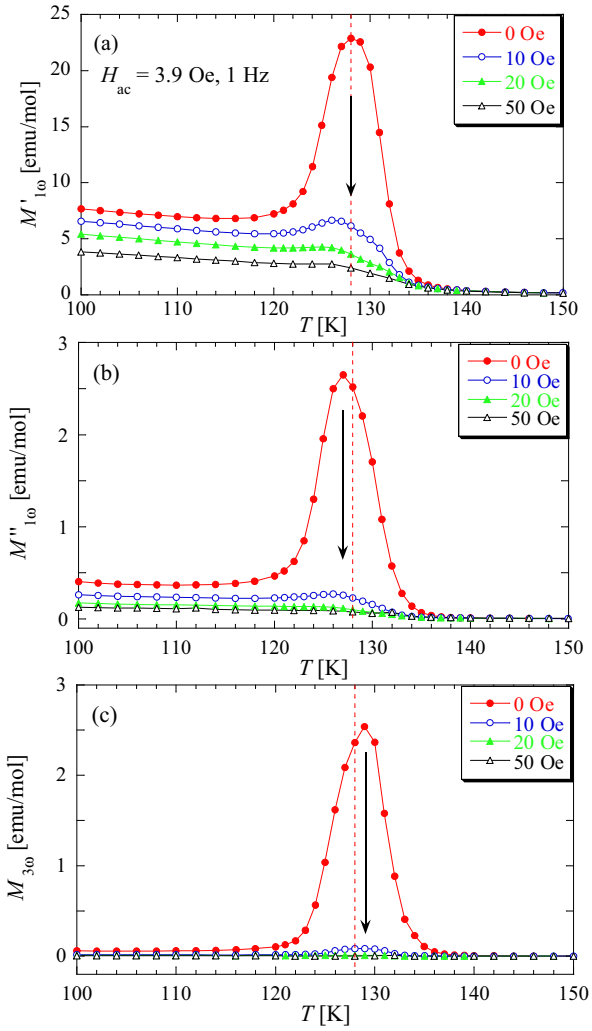

FIG. 2. Temperature dependence of ac magnetic responses (a) $M'_{1\omega}$, (b) $M''_{1\omega}$, and (c) $M_{3\omega}$ for $Cr_{1/3}NbS_2$ under an ac field with $h = 3.9$ Oe and $f = 1$ Hz for $H_{dc} = 0$, 10, 20, and 50 Oe. A series of ac responses corresponds to the magnetic response near [A] in Fig. 8. Red dotted lines, which represent the temperature with the maximum $M'_{1\omega}$ at $H_{dc} = 0$, are guides for the eyes. Arrows in (a), (b), and (c) indicate the direction of the change in $M'_{1\omega}$, $M''_{1\omega}$, and $M_{3\omega}$, respectively.

$M_{3\omega}$ observed at $T = 129$ K is approximately on the order of 8% of $M_{1\omega}$. The Klirr factor, $M_{3\omega}/M_{1\omega}$, increases as the amplitude of H_{ac} increases, reaching 10.8% at $h = 3.9$ Oe (see Fig. 2). The Klirr factor depends sensitively on the crystal quality and decreases in poorly crystalline samples with lower T_c. To our knowledge, the Klirr factor at the 10% level is one of the largest Klirr factors observed to date [19,29,30], suggesting that the $M(t)$ response is quite distorted. Thus, the magnetic dynamics at around T_c indicates intrinsic magnetic nonlinearity.

Given the phenomenological evidence, a large magnetic nonlinearity is often observed near T_c in the crystal group allowing the D-M interaction (including locally permitted D-M vectors as well as a uniform D-M vector over the entire crystal). The present case is consistent with this framework, so we are confident that the present measurement detects the magnetic response of the macroscopic chiral spin coherence over the entire crystal. The anomaly in $M_{3\omega}$ shifts slightly toward the low-temperature side as the frequency of H_{ac} increases, as seen in Fig. 1(c). A series of h and f dependencies indicates that the giant nonlinear magnetic response is quite steady in the considered region of $f \leqslant 500$ Hz.

A few materials with ferromagnetic interaction and D-M vectors often have large Klirr factors (at the 10% level) at zero dc field [19,29,30]. In the future, when similar studies of typical helical magnetic systems are conducted, one could provide a typical value of the Klirr factor for typical helical magnets; however, we suppose that the Klirr factor for a monoaxial D-M vector system such as $Cr_{1/3}NbS_2$ would be much larger than that for a multiaxial D-M vector system such as MnSi.

B. At finite dc field

Theoretically, under a finite H_{dc} applied perpendicular to the chiral axis, the HM structure is transformed to the CSL state. Figures 2 and 3 show $M'_{1\omega}$ (a), $M''_{1\omega}$ (b), and $M_{3\omega}$ (c) under an ac field with $h = 3.9$ Oe and $f = 1$ Hz for $H_{dc} =$ 0–50 Oe (Fig. 2) and 0.2–2.2 kOe (Fig. 3). As seen in Fig. 2(c), the giant $M_{3\omega}$ decreases dramatically with increasing H_{dc}, and, when H_{dc} exceeds a few tens of oersteds, $M_{3\omega}$ disappears. However, $M_{3\omega}$ reappears at $H_{dc} \geqslant 1$ kOe [Fig. 3(c)].

Figure 3(a) indicates that the anomaly in $M'_{1\omega}$ is split, and the splitting becomes more prominent with increasing H_{dc}. The anomaly in $M'_{1\omega}$ on the high-temperature side [$M'_{1\omega}$ (HT)] shifts slightly toward higher temperatures with increasing H_{dc}, and the magnitude gradually decreases. However, for $H_{dc} \geqslant$ 1.4 kOe, the anomaly changes very little in magnitude. On the other hand, the anomaly in $M'_{1\omega}$ on the low-temperature side [$M'_{1\omega}$ (LT)] shifts remarkably toward lower temperatures with increasing H_{dc}, and the change in the magnitude is temporarily enhanced but later suppressed. Next, Fig. 3(b) indicates that the anomaly in $M''_{1\omega}$ follows that in $M'_{1\omega}$ (LT), and the H_{dc} dependence of $M''_{1\omega}$ is consistent with that of $M'_{1\omega}$ (LT). Thus, the anomaly in $M'_{1\omega}$ (LT) is accompanied by energy loss in the domain dynamics under H_{ac}, whereas that of $M'_{1\omega}$ (HT) responds linearly without energy loss. This $M'_{1\omega}$ (HT) appears on the boundary between the FFM and PM states without $M_{3\omega}$. However, $M_{3\omega}$ reappears on the curve that accompanies both $M'_{1\omega}$ (LT) and $M''_{1\omega}$ (LT) after the temporary disappearance at $H_{dc} = 0.02$–0.6 kOe. This attractive curve is consistent with the boundary between the CSL and FFM states.

Figures 4–6 show the frequency dependence of the ac magnetic responses $M'_{1\omega}$, $M''_{1\omega}$, and $M_{3\omega}$ for $Cr_{1/3}NbS_2$ at $H_{dc} = 0.2$, 1.0, and 1.6 kOe, respectively. These frequency dependencies show that the intrinsic nature of the magnetic dynamics at $H_{dc} = 0.2$ and 1.0 kOe does not change greatly with f and is similar to steady behavior observed at $H_{dc} = 0$. Indeed, the dynamics at $H_{dc} = 0.2$ kOe is not accompanied by $M_{3\omega}$, whereas that at $H_{dc} =$ 1.0 kOe is. Their magnetic origins differ from each other, whereas the magnetic dynamics in both cases is steady against the change in f. This rigidness is also seen in $M'_{1\omega}$ (HT) at $H_{dc} = 1.6$ kOe [Fig. 6(a)]. Thus, the magnetic dynamics, the high-temperature side of which consists of the PM state, is rigid against H_{ac}. However, $M'_{1\omega}$ (LT) at $H_{dc} = 1.6$ kOe is

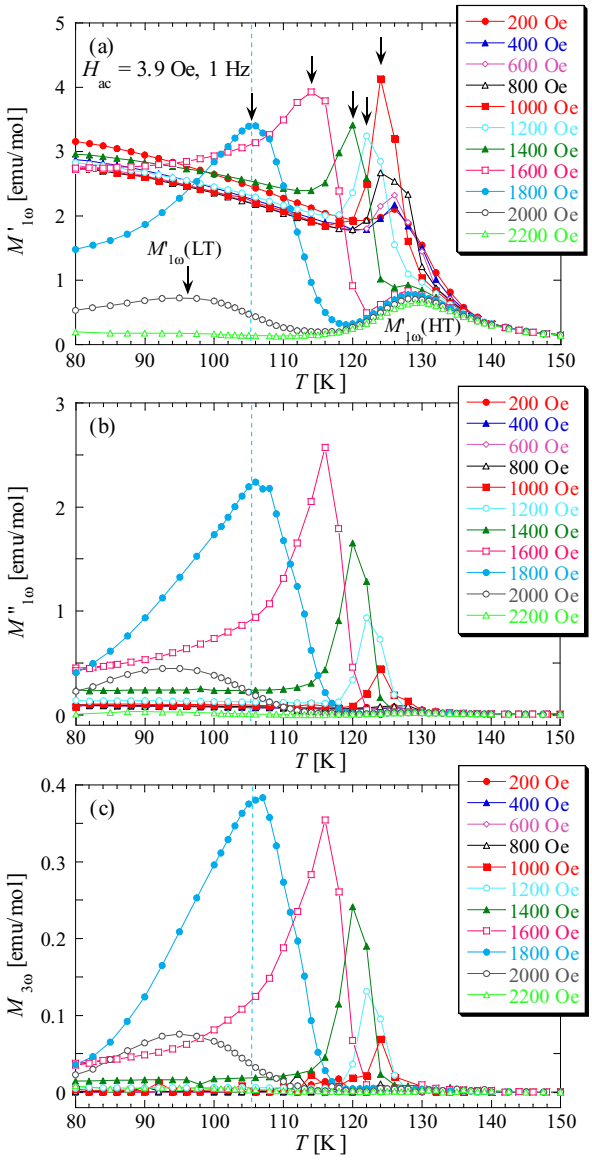

FIG. 3. Temperature dependence of ac magnetic responses (a) $M'_{1\omega}$, (b) $M''_{1\omega}$, and (c) $M_{3\omega}$ for $Cr_{1/3}NbS_2$ under an ac field with h = 3.9 Oe and f = 1 Hz at H_{dc} = 0.2–2.2 kOe. Light blue dotted lines, which represent the temperature with the maximum $M'_{1\omega}$ at H_{dc} = 1.8 kOe, are guides for the eyes. Arrows in (a) indicate the anomaly $M'_{1\omega}$ (LT).

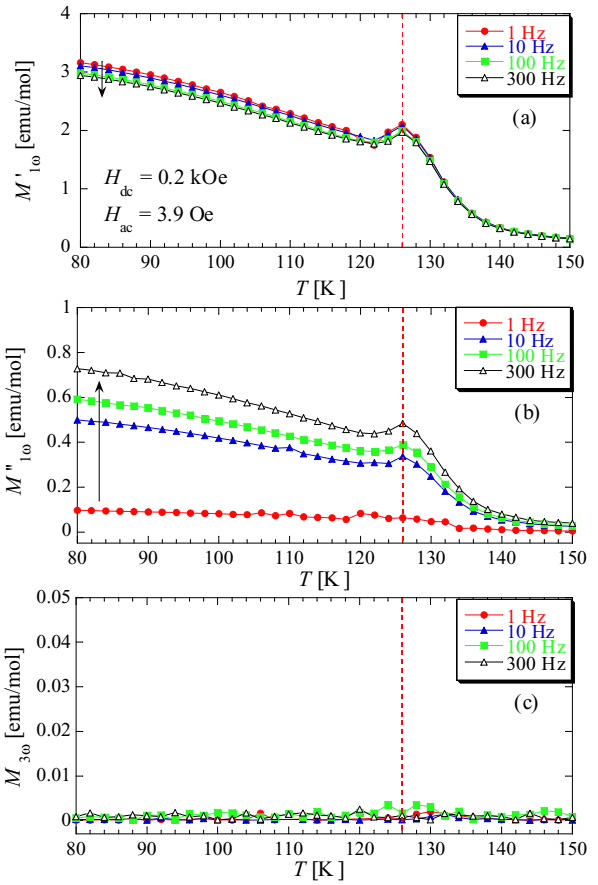

FIG. 4. Temperature dependence of ac magnetic response (a) $M'_{1\omega}$, (b) $M''_{1\omega}$, and (c) $M_{3\omega}$ for $Cr_{1/3}NbS_2$ under an ac field with h = 3.9 Oe and f = 1–300 Hz at H_{dc} = 0.2 kOe. A series of ac responses corresponds to the magnetic response [B] in Fig. 8. Red dotted lines, which represent the temperature with the maximum $M'_{1\omega}$, are guides for the eyes. Arrows in (a) and (b) indicate the direction of the change in $M'_{1\omega}$ and $M''_{1\omega}$, respectively.

suppressed with increasing f, and this characteristic is also observed in both $M''_{1\omega}$ and $M_{3\omega}$. The corresponding magnetic dynamics is on the boundary between the CSL and FFM states. These results tell us that there are experimentally two CSL states depending on H_{dc}.

Indeed, we have measured the ac magnetic response under zero dc field and some finite dc fields such as 0.2, 1.0, and 1.6 kOe, although we could not find any characteristic anomaly at around 50 K. We think that it might be difficult to detect any behavior related to the change in magnetic structure [16] and/or the change in the stable spin orientation [17] by studying the magnetic dynamics against an ac field of a few oersteds at most.

C. Phase diagram

In this subsection, the phase diagram as a function of H_{dc} and T is constructed. Thus, the $M-H_{dc}$ curve as a function of T was observed, and the result [Fig. 7(a)] is almost the same as the data in the literature [7,8]. The critical field (H_c) for the transition from the CSL state to the FFM state and the upper limit of the magnetically linear region (H_L) at T = 50 K are indicated by arrows. Indeed, the low H_{dc} region does not exhibit perfect linearity. Thus, we define H_L at the value of which the change in dM/dH_{dc} becomes prominent [see Fig. 7(b)], where the value of H_L was determined from the data of d^2M/dH_{dc}^2 [see Fig. 7(c)]. Figure 8 presents the (T, H_{dc}) coordinates at which the anomalies in $M'_{1\omega}$, $M''_{1\omega}$, and $M_{3\omega}$ are observed. The temperature dependence of H_c and H_L is also summarized in Fig. 8, along with the above information, in order to classify the CSL state into two regions such as CSL-1 and CSl-2. Furthermore, the data of the phase boundary determined by magnetoresistance measurements for the microsample with $H_c < 2$ kOe [18] are also plotted there. The phase boundaries obtained here include both information

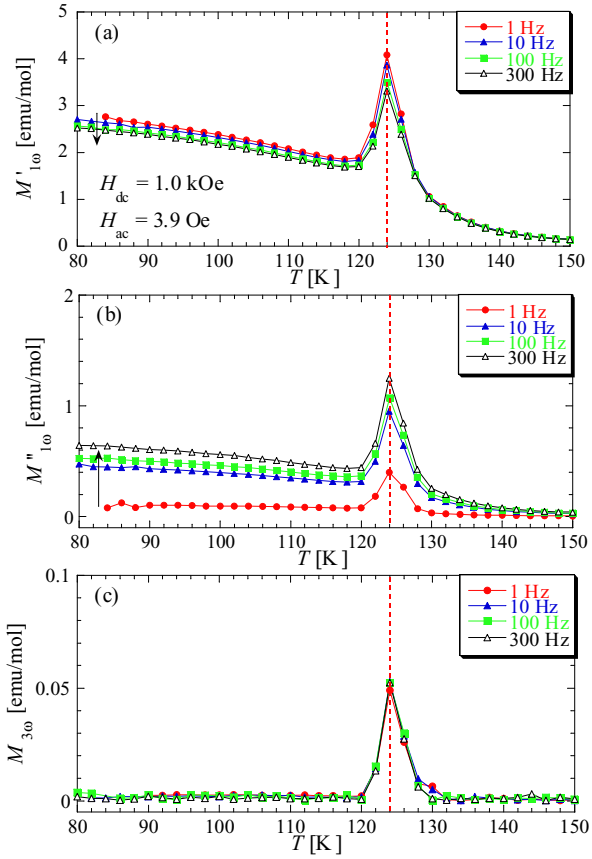

FIG. 5. Temperature dependence of ac magnetic response (a) $M'_{1\omega}$, (b) $M''_{1\omega}$, and (c) $M_{3\omega}$ for $Cr_{1/3}NbS_2$ under an ac field with $h = 3.9$ Oe and $f = 1$–300 Hz at $H_{dc} = 1.0$ kOe. A series of ac responses corresponds to the magnetic response [C] in Fig. 8. Red dotted lines, which represent the temperature with the maximum $M'_{1\omega}$, are guides for the eyes. Arrows in (a) and (b) indicate the direction of the change in $M'_{1\omega}$ and $M''_{1\omega}$, respectively.

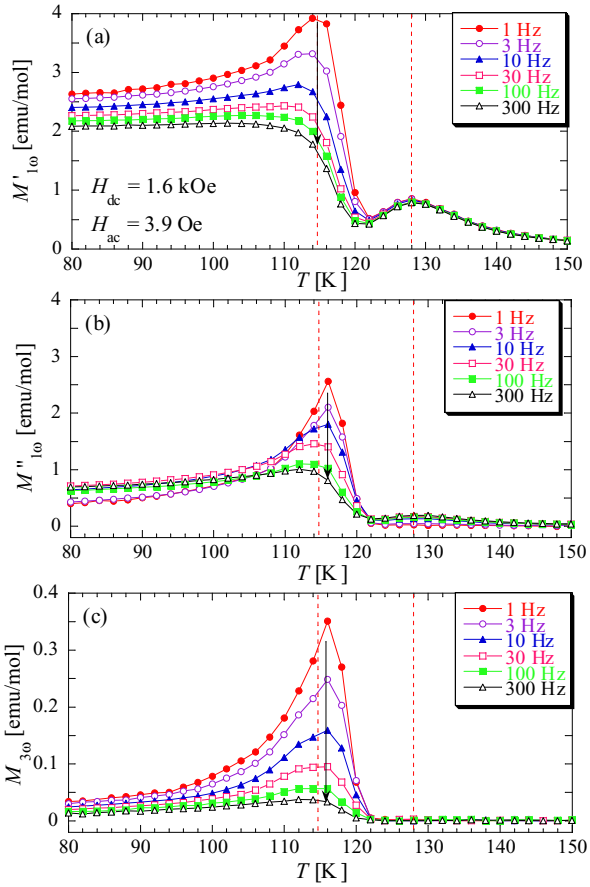

FIG. 6. Temperature dependence of ac magnetic response (a) $M'_{1\omega}$, (b) $M''_{1\omega}$, and $M_{3\omega}$ for $Cr_{1/3}NbS_2$ under an ac field with $h = 3.9$ Oe and $f = 1$–300 Hz at $H_{dc} = 1.6$ kOe. A series of ac responses corresponds to the magnetic responses [D] and [E] in Fig. 8. Red dotted lines, which represent the temperatures with the maximum $M'_{1\omega}$ at $f = 1$ Hz, are guides for the eyes.

from the magnetoresistance measurement [18] and that from the magnetization curve [14].

At $H_{dc} = 0$, the HM state is transformed to the PM state at point A, where a giant $M_{3\omega}$ of $M_{3\omega}/M_{1\omega} \geqslant 0.1$ ($h = 3.9$ Oe) appears. Here coherent long-range helicity exists over the entire crystal. However, a small H_{dc} applied perpendicular to the chiral axis destroys this long-range helical coherence and causes the CSL to appear, so the collapse of coherent helicity is connected with the disappearance of $M_{3\omega}$. We stress that point A is just the singularity. In the CSL state under small H_{dc} (termed CSL-1), a helical array with 2π rotation of the spin phase is richer than the ferromagnetic array. In the M-H_{dc} curve, this CSL-1 region corresponds to the region exhibiting linearity between M and H_{dc}. Indeed, the H_L value in Fig. 7 coincides with a point near C in Fig. 8, where an anomaly in $M'_{1\omega}$ splits into two anomalies. This existence of a boundary in the CSL was not confirmed in the magnetoresistance measurement, which detects the electrical conductivity of the Nb and S atoms. At higher H_{dc}, another CSL state, CSL-2, appears; its superlattice consists of ferromagnetic arrays connected by a type of node constructed by 2π rotation of the spin phase. As the temperature increases, thermal fluctuation stabilizes the FMM state rather than the CSL-2 state, and there a large $M_{3\omega}$ reappears. Phase coherence due to the ferromagnetic array rather than the helicity becomes richer with increasing H_{dc}. It responds strongly to H_{ac}, causing hysteresis in M versus H_{dc} as well as in M versus H_{ac}. A further increase in the temperature transforms the FFM state to the PM state. This change has also been observed in the magnetoresistance measurement [18]. This FFM-PM transition exhibits a nearly linear response, like the CSL-1–PM transition, and was not observed in the M-H_{dc} measurements. The transformation from CSL-1 to CSL-2 would be a type of crossover, resulting in no anomaly in the ac response (e.g., the low-temperature side of point C in Fig. 8). The straightness from point C to point A in the phase diagram of Fig. 8 is also seen in the H_{dc}-T phase diagram of MnSi, where the phase boundary is in the high-temperature side of the skyrmion phase [33,34]. The phase boundary presents the first-order transition accompanying the tri-critical point [33,34]. The phase boundary between CSL-1 and PM in $Cr_{1/3}NbS_2$, without $M_{3\omega}$, can be the first-order transition.

In the next section, the magnetic dynamics at five representative points (A–E) in Fig. 8 is classified into several types, according to the procedure described in Ref. [19].

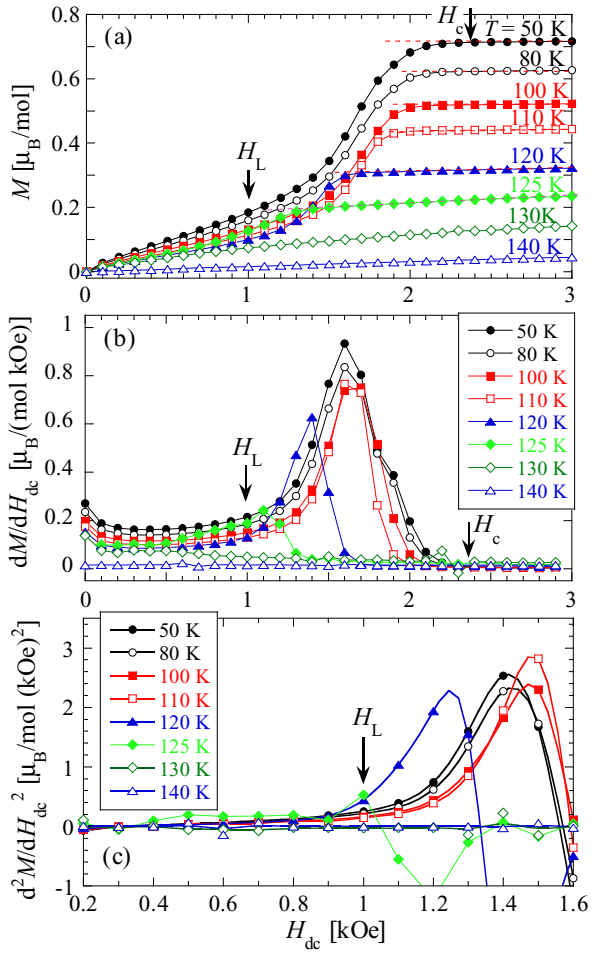

FIG. 7. Magnetization curve of $Cr_{1/3}NbS_2$ at $T = 50$, 80, 100, 110, 120, 125, 130, and 140 K (a), along with the first-order (b) and the second-order differentiation (c) of M with the respect to the dc field H_{dc}. In (a), broken lines represent the saturation moment at each temperature ($T \leqslant 120$ K). In (a)–(c), some arrows present the saturation field H_c and the upper limit of the linear response ($dM/dH_{dc} \sim$ const.) H_L at $T = 50$ K. In (c), H_L is defined as the field above which d^2M/dH_{dc}^2 begins to increase.

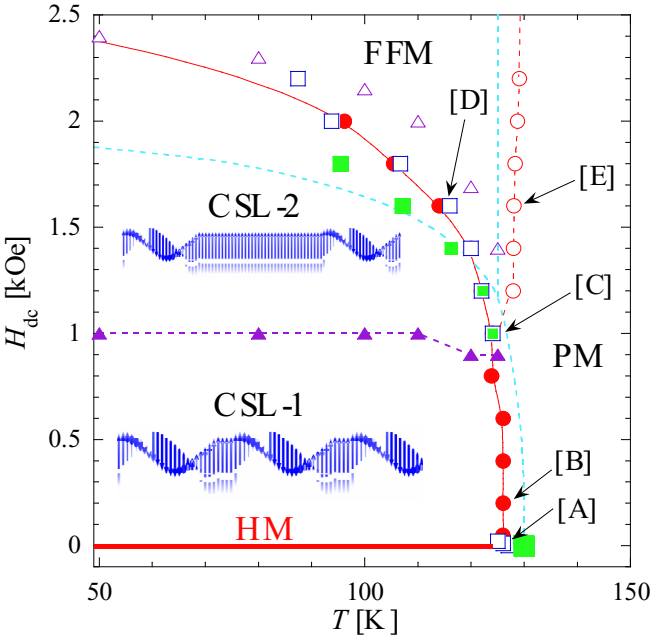

FIG. 8. Phase (region) diagram of $Cr_{1/3}NbS_2$ under the dc magnetic field H_{dc}. A series of anomalies observed in the ac magnetic susceptibility measurements such as $M'_{1\omega}$ (●, ○), $M''_{1\omega}$ (□), and $M_{3\omega}$ (■) is plotted. The intensity of the $M_{3\omega}$ anomaly is symbolized by the size of the symbol. The characteristic changes detected in the M-H curve of Fig. 7, characterized by H_c (△) and H_L (▲), are presented, along with the data on the regional boundary determined by magnetoresistance measurements for the microsample with $H_c < 2$ kOe (light blue dotted curve and line) [18]. Dotted line connecting the H_L data (▲) marks the crossover from the magnetically linear region to the nonlinear region; we stress that it does not represent the phase boundary. Each region is characterized as HM, CSL-1, CSL-2, FFM, and PM, respectively. For $H_{dc} = 0$, 0.2, 1.0, and 1.6 kOe, there are five points, A–E, that exist on attractive boundaries as A, HM → PM; B, CSL-1 → PM; C, CSL-2 → (FFM →) PM; D, CSL-2 → FFM; E, FFM → PM. The magnetic hysteresis at each point is analyzed in Fig. 9.

IV. DISCUSSION

Replacing M as a function of t with M as a function of H_{ac} yields a picture of the dynamical magnetic hysteresis (ac hysteresis hereafter), providing quantitative information on the nonlinearity related to $M_{3\omega}$. Figure 9 shows M (H_{ac}) for points A–E in Fig. 8.

In the ac hysteresis measurement, some types of hysteresis loops appear, the shape of which depends on the magnitude of the nonlinearity as well as that of the damping. In the previous study of MnP, we systematized the $M(H)$ loop using the following equivalent mechanical equation for the magnetic domain motion [19]:

$$\frac{d^2x}{dt^2} + 2\gamma\frac{dx}{dt} + \omega_0^2 x + \eta x^3 = F\sin\omega t, \qquad (2)$$

where x is the position of the material (here, a DW) with a mass m connected to a spring with spring constant k [32]. Equation (2) is the familiar mechanical nonlinear spring equation in the field of mechanics, termed the Duffing equation. Recently, Kishine *et al.* have theoretically pointed out that the dynamics of the weakly pinned CSL in a monoaxial chiral helimagnet is described by the effective Lagrangian of the modified Duffing oscillator model [35]. The first term on the left-hand side of Eq. (2) represents the inertia of the DW. The second term represents any damping, and γ denotes the magnitude of the friction that originates in the eddy current in a metal. The elasticity, characterized by k, is physically related to a pinning effect, so $\omega_0 = (k/m)^{1/2}$. In a magnetic sense, ω_0 should be connected to the predominant magnetic anisotropy as well as defects and/or imperfections. Here, the coefficient of the x^3 term η represents the existence of multiple spring constants depending on the region of displacement, and it has a nonlinear effect in its narrow meaning, accompanied by a change in the shape of the hysteresis loop. In the present magnetic study, the term on the right-hand side, $F\sin\omega t$, is replaced by the ac field, $h\sin\omega t$; furthermore, x is replaced by the magnetization M (more precisely, the deviation from the magnetization in the equilibrium state). Indeed, Eq. (2) without

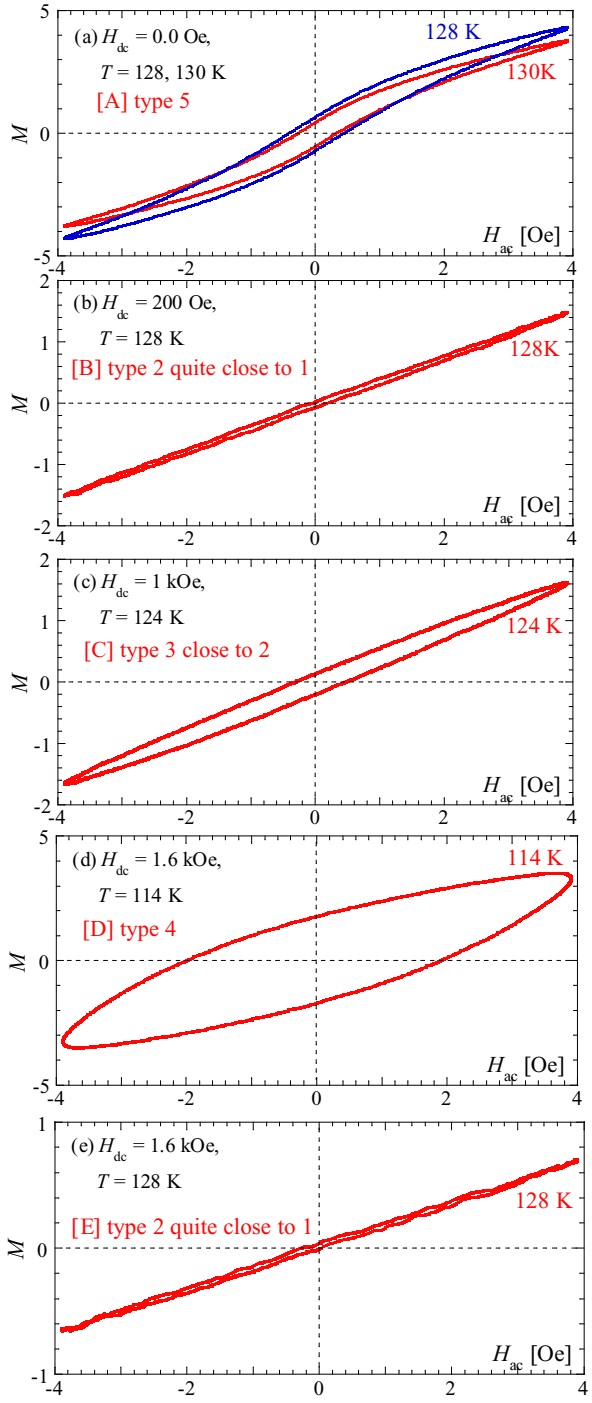

FIG. 9. Ac magnetic hysteresis for five (T, H_{dc}) points: A (128–130 K, 0 kOe), B (128 K, 0.2 kOe), C (124 K, 1.0 kOe), D (114 K, 1.6 kOe), and E (128 K, 1.6 kOe). In Table II, these magnetic dynamics are classified by analyzing M vs H_{ac} and M vs t according to a procedure described elsewhere [19].

the ηx^3 term cannot produce $M_{3\omega}$ [19]. In the previous study of MnP, we classified the typical responses into five groups, as shown in Table I [19]; types 1 and 2 appear for $\eta = 0$, and type 1 further requires $\gamma = 0$. As γ increases, the types are transformed as $3 \rightarrow 4 \rightarrow 5$.

We characterize the magnetic responses observed at five (T, H_{dc}) points: A (128–130 K, 0 kOe), B (128 K, 0.2 kOe), C (124 K, 1.0 kOe), D (114 K, 1.6 kOe), and E (128 K, 1.6 kOe) (see Table II). The characteristic ac hysteresis at A appears only in a narrow region, suggesting a remarkable $M_{3\omega}$; this ac response at A is of type 5. Point A is just the singularity with the long-range order of helical spin phase. $M_{3\omega}$ disappears when H_{dc} is applied, and it reappears at $H_{dc} \geqslant 1$ kOe owing to stabilization of CSL-2. The linear ac response at B [CSL-1 $\rightarrow$ (FFM $\rightarrow$) PM] is quite similar to that at E [FFM $\rightarrow$ PM]. Near C, the ac hysteresis starts to expand, and $M_{3\omega}$ is enlarged; this ac response at C is of type 3 close to type 2. The response at D has a wide ac hysteresis, and $M_{3\omega}$ is also large; this ac response at D is of type 4, suggesting that the energy loss against the change in H_{ac} is prominent. Thus, the difference between B and D suggests that the helicity-rich CSL-1 state differs from the ferromagnetic-array-rich CSL-2 state in terms of the magnetic dynamics under H_{ac}. Furthermore, a series of magnetic responses following A $\rightarrow$ B $\rightarrow$ C $\rightarrow$ E is rigid against H_{ac}, resulting in little energy loss with changing H_{ac}.

The theory of the CSL is based entirely on the Ginzburg-Landau formalism, in which the energy density does not contain any source of discontinuous phase transitions [4]. The hysteresis phenomena are concomitant with the discontinuous (first-order) phase transition, which requires additional terms (a third-order term with respect to the order parameter, for example). Thus, the absence of hysteresis is fairly consistent with the theory. Furthermore, there is not any theory which well describes low-frequency collective dynamics in the CSL phase. One approach to treating this problem is to take account of low-frequency excitations around the CSL state, which are analogous to DW oscillation over semimacroscopic length scales. Clarification of this mechanism is an ongoing issue.

TABLE I. Typical ac response according to the procedure proposed in Ref. [19].

Type	$M_{3\omega}/M_{1\omega}$	H_c/h	$M''_{1\omega}/M'_{1\omega}$	γ	η
1	0	0	0	0	0
2	0	$\neq 0$	$\neq 0$	$\neq 0$	0
3	<0.05	>0.5	$\neq 0$	$\neq 0$	$\neq 0$
4	$\geqslant 0.05$	>0.1	$\neq 0$	$\neq 0$	$\neq 0$
5	$\geqslant 0.05$	$\leqslant 0.1$	~ 0	$\neq 0$	$\neq 0$

TABLE II. Magnetic diagnostics for $Cr_{1/3}NbS_2$ under ac field with $h = 3.9$ Oe and $f = 1$ Hz. The diagnostics is conducted for five (T, H_{dc}) points: A (128–130 K, 0 kOe), B (128 K, 0.2 kOe), C (124 K, 1.0 kOe), D (114 K, 1.6 kOe), and E (128 K, 1.6 kOe).

Object	Transition	$M_{3\omega}/M_{1\omega}$	H_c/h	Type
A	HM $\rightarrow$ PM	0.11	<0.10	5
B	CSL-1 $\rightarrow$ PM	0.00	0.03	2 close to 1
C	CSL-2 $\rightarrow$ FFM $\rightarrow$ PM	0.02	0.09	3 close to 2
D	CSL-2 $\rightarrow$ FFM	0.09	0.47	4
E	FFM $\rightarrow$ PM	0.00	0.01	2 close to 1

V. CONCLUSION

We constructed the phase (region) diagram of the chiral magnet $Cr_{1/3}NbS_2$ as a function of T and H_{dc} using ac magnetic susceptibility measurements of a single crystal. The obtained phase (region) diagram includes physical information from both the magnetoresistance and magnetization curve measurements. In terms of the magnetic dynamics, the CSL state is divided into two regions, the helicity-rich CSL-1 and ferromagnetic-array-rich CSL-2. The transition from CSL-2 to the FFM state is accompanied by a nonlinear response and a large energy loss, whereas that from the FFM state to the PM state exhibits a linear magnetic response without any energy loss. The transition from CSL-1 to the PM state has qualitatively the same nature as the FFM-PM transition. We stress that the largest $M_{3\omega}$ appears at the HM-PM transition, and H_{dc} suppresses $M_{3\omega}$ in CSL-1. However, in CSL-2, the development of the ferromagnetic array causes an $M_{3\omega}$ originating from the reappearance of the finite-range spin coherence due to the ferromagnetic array. The reappearance of a nonlinear contribution on the boundary between CSL-2 and the FFM state surely originates from the magnetic superlattice consisting of an adequate ferromagnetic array and periodic spin helicity in CSL-2; the ferromagnetic array is locked on the lattice via the spin helicity due to the D-M interaction. Thus, the magnetic diagnostics on the phase boundaries reveals that CSL-1 is a very light superlattice without energy loss against the ac field, whereas CSL-2 is heavy, with hysteresis in the M-H_{dc} curve.

ACKNOWLEDGMENTS

This work was supported by Grants-in-Aid for Scientific Research, Grants No. (A) 22245023 and No. (S) 25220803, from the Ministry of Education, Culture, Sports, Science and Technology (MEXT), Japan. This work was also supported by the Center for Chiral Science in Hiroshima University (the MEXT program for promoting the enhancement of research universities, Japan) and JSPS Core-to-Core Program, Advanced Research Networks.

[1] I. E. Dzyaloshinskii, Sov. Phys. JETP **5**, 1259 (1957).
[2] T. Moriya, Phys. Rev. **120**, 91 (1960).
[3] I. E. Dzyaloshinskii, Sov. Phys. JETP **20**, 665 (1965).
[4] J. Kishine, K. Inoue, and Y. Yoshida, Prog. Theor. Phys. Suppl. **159**, 82 (2005).
[5] I. G. Bostrem, J. Kishine, and A. S. Ovchinnikov, Phys. Rev. B **77**, 132405 (2008).
[6] I. G. Bostrem, J. Kishine, and A. S. Ovchinnikov, Phys. Rev. B **78**, 064425 (2008).
[7] T. Miyadai, K. Kikuchi, H. Kondo, S. Sakka, M. Arai, and Y. Ishikawa, J. Phys. Soc. Jpn. **52**, 1394 (1983).
[8] Y. Togawa, T. Koyama, K. Takayanagi, S. Mori, Y. Kousaka, J. Akimitsu, S. Nishihara, K. Inoue, A. S. Ovchinnikov, and J. Kishine, Phys. Rev. Lett. **108**, 107202 (2012).
[9] A. R. Beal, in *Intercalated Layered Materials*, edited by F. A. Levy (D. Reidel Publishing, Dordecht, 1979).
[10] F. Hulliger and E. V. A. Pobitschka, J. Solid State Chem. **1**, 117 (1970).
[11] L. M. Volkova and D. V. Marinin, J. Appl. Phys. **116**, 133901 (2014).
[12] M. Mito, T. Tajiri, K. Tsuruta, H. Deguchi, J. Kishine, K. Inoue, Y. Kousaka, Y. Nakao, and J. Akimitsu, J. Appl. Phys. **117**, 183904 (2015).
[13] H. Matsuura (private communication).
[14] N. J. Ghimire, M. A. McGuire, D. S. Parker, B. Sipos, S. Tang, J.-Q. Yan, B. C. Sales, and D. Mandrus, Phys. Rev. B **87**, 104403 (2013).
[15] M. Mito, S. Tominaga, Y. Komorida, H. Deguchi, S. Takagi, Y. Nakao, Y. Kousaka, and J. Akimitsu, J. Phys: Conf. Ser. **215**, 012182 (2010).
[16] D. Braam, C. Gomez, S. Tezok, E. V. L. de Mello, L. Li, D. Mandrus, H.-Y. Kee, and J. E. Sonier, Phys. Rev. B **91**, 144407 (2015).
[17] A. C. Bornstein, B. J. Chapman, N. J. Ghimire, D. G. Mandrus, D. S. Parker, and M. Lee, Phys. Rev. B **91**, 184401 (2015).
[18] Y. Togawa, Y. Kousaka, S. Nishihara, K. Inoue, J. Akimitsu, A. S. Ovchinnikov, and J. Kishine, Phys. Rev. Lett. **111**, 197204 (2013).
[19] M. Mito, H. Matsui, K. Tsuruta, H. Deguchi, J. Kishine, K. Inoue, Y. Kousaka, S. Yano, Y. Nakao, and J. Akimitsu, J. Phys. Soc. Jpn. **84**, 104707 (2015).
[20] M. Suzuki, Prog. Theor. Phys. **58**, 1151 (1977).
[21] S. Fujiki and S. Katsura, Prog. Theor. Phys. **65**, 1130 (1981).
[22] Y. Miyako, S. Shikazawa, T. Saito, and Y. G. Yuochunas, J. Phys. Soc. Jpn. **46**, 1951 (1979).
[23] T. Bitoh, T. Shirane, and S. Chikazawa, J. Phys. Soc. Jpn. **62**, 2837 (1993).
[24] T. Shirane, T. Moiya, T. Bitoh, A. Sawada, H. Aida, and S. Chikazawa, J. Phys. Soc. Jpn. **64**, 951 (1995).
[25] T. Shirane and S. Sakurai, J. Korean Phys. Soc. **62**, 2173 (2013).
[26] M. Mito, M. Ogawa, H. Deguchi, M. Yamashita, and H. Miyasaka, J. Appl. Phys. **107**, 124316 (2010).
[27] M. Mito, M. Ogawa, H. Deguchi, M. Yamashita, and H. Miyasaka, J. Phys. Soc. Jpn. **81**, 064716 (2012).
[28] M. Mito, K. Iriguchi, Y. Taniguchi, M. Kawase, S. Takagi, and H. Deguchi, J. Phys. Soc. Jpn. **80**, 064707 (2011).
[29] M. Mito, K. Iriguchi, H. Deguchi, J. Kishine, K. Kikuchi, H. Osumi, Y. Yoshida, and K. Inoue, Phys. Rev. B **79**, 012406 (2009).
[30] M. Mito, K. Iriguchi, H. Deguchi, J. Kishine, Y. Yoshida, and K. Inoue, J. Appl. Phys. **111**, 103914 (2012).
[31] T. Liu, H. Zheng, S. Kang, Y. Shiota, S. Hayami, M. Mito, O. Sato, K. Yoshizawa, S. Kanegawa, and C. Duan, Nat. Commun. **4**, 2826 (2013).
[32] S. Chikazumi, *Physics of Ferromagnets* (Oxford University Press, New York, 1997).
[33] A. Bauer and C. Pfleiderer, Phys. Rev. B **85**, 214418 (2012).
[34] L. Zhang, D. Menzel, C. Jin, H. Du, M. Ge, C. Zhang, L. Pi, M. Tian, and Y. Zhang, Phys. Rev. B **91**, 024403 (2015).
[35] J. Kishine, I. Proskurin, I. G. Bosterm, A. S. Ovchinnikov, and V. E. Sinitsyn, Phys. Rev. B **93**, 054403 (2016).